Atmos. Meas. Tech. Discuss., 8, 405–441, 2015
www.atmos-meas-tech-discuss.net/8/405/2015/
doi:10.5194/amtd-8-405-2015

Atmospheric Measurement Techniques Discussions

Profiling wind and greenhouse gases by infrared-laser occultation: algorithm and results from end-to-end simulations in windy air

A. Plach, V. Proschek, and G. Kirchengast

Wegener Center for Climate and Global Change (WEGC) and Institute for Geophysics, Astrophysics and Meteorology/Institute of Physics (IGAM/IP), University of Graz, Graz, Austria

Received: 31 October 2014 – Accepted: 8 December 2014 – Published: 12 January 2015

Correspondence to: A. Plach (andreas.plach@uni-graz.at)

Published by Copernicus Publications on behalf of the European Geosciences Union.

Abstract

The new mission concept of microwave and infrared-laser occultation between low-Earth-orbit satellites (LMIO) is designed to provide accurate and long-term stable profiles of atmospheric thermodynamic variables, greenhouse gases (GHGs), and line-of-sight (l.o.s.) wind speed with focus on the upper troposphere and lower stratosphere (UTLS). While the unique quality of GHG retrievals enabled by LMIO over the UTLS has been recently demonstrated based on end-to-end simulations, the promise of l.o.s. wind retrieval, and of joint GHG and wind retrieval, has not yet been analyzed in any realistic simulation setting so far. Here we describe a newly developed l.o.s. wind retrieval algorithm, which we embedded in an end-to-end simulation framework that also includes the retrieval of thermodynamic variables and GHGs, and analyze the performance of both standalone wind retrieval and joint wind and GHG retrieval. The wind algorithm utilizes LMIO laser signals placed on the inflection points at the wings of the highly symmetric $C^{18}OO$ absorption line near 4767 cm^{-1} and exploits transmission differences from wind-induced Doppler shift. Based on realistic example cases for a diversity of atmospheric conditions, ranging from tropical to high-latitude winter, we find that the retrieved l.o.s wind profiles are of high quality over the lower stratosphere under all conditions, i.e., unbiased and accurate to within about 2 $m\,s^{-1}$ over about 15 to 35 km. The wind accuracy degrades into the upper troposphere due to decreasing signal-to-noise ratio of the wind-induced differential transmission signals. The GHG retrieval in windy air is not vulnerable to wind speed uncertainties up to about 10 $m\,s^{-1}$ but is found to benefit in case of higher speeds from the integrated wind retrieval that enables correction of wind-induced Doppler shift of GHG signals. Overall both the l.o.s. wind and GHG retrieval results are strongly encouraging towards further development and implementation of a LMIO mission.

AMTD
8, 405–441, 2015

1 Introduction

This study is based on the mission concept ACCURATE – climate benchmark profiling of greenhouse gases and thermodynamic variables and wind from space (Kirchengast et al., 2010). The ACCURATE concept utilizes inter-satellite crosslinks between low Earth orbit (LEO) satellites and represents a synergistic combination of the LEO-LEO microwave occultation (LMO) and the LEO-LEO infrared-laser occultation (LIO) technique. LMO is used to derive thermodynamic state variables, like pressure (p), temperature (T) and humidity (q). Performed simultaneously from the same receiver (Rx) and transmitter (Tx) platforms as the LMO, the LIO is utilized to retrieve greenhouse gas (GHG) trace species concentrations and line-of-sight (l.o.s.) wind speed. The combined LEO-LEO microwave and infrared-laser occultation method (LMIO) is already well investigated and has undergone a range of studies introducing the concept and analyzing its feasibility and performance (Schweitzer, 2010; Kirchengast and Schweitzer, 2011; Schweitzer et al., 2011b, a; Proschek et al., 2011, 2014). In mission pre-development context it received positive evaluation, encourging further studies, as part of the Earth Explorer 8 (EE8) mission call (Kirchengast et al., 2010) from the European Space Agency (ESA).

The LMIO method, introduced by Kirchengast and Schweitzer (2011), is a next-generation step in the development of the well established and meanwhile widely used radio occultation (RO) method which operates in the L-band region (Ware et al., 1996; Kursinski et al., 1997). In contrary to RO, LMIO utilizes a LEO satellite actively transmitting limb-sounding microwave (MW) and infrared-laser (IR) signals to a receiving LEO satellite. This setup is capable of providing independent, self-calibrated long-term stable measurements with high vertical resolution for climate monitoring and research (Kirchengast and Schweitzer, 2011).

The IR-signals operate best under clear air conditions, which means no influence of clouds but of other atmospheric broadband effects like defocusing loss (Kursinski et al., 2000), Rayleigh scattering (Salby, 2012), aerosol extinction (Salby, 1996; Liou,

AMTD
8, 405–441, 2015

2002), and scintillations (Andrews and Philips, 2005; Gurvich et al., 2012). Schweitzer et al. (2011b) have analyzed these clear air influences in detail and Proschek et al. (2011) have studied the GHG retrieval performance under these conditions. Recently Proschek et al. (2014) also have carefully studied the influences of clouds and how retrievals successfully perform over broken cloudiness. In this study we use the clear-air conditions as context, since we focus on the integrated retrieval also of l.o.s. wind speed, which has its core range of application in the lower stratosphere from about 15 km upwards above the typical tropospheric cloudiness. Only initial simplified studies regarding the l.o.s. wind speed retrieval are available so far (Schweitzer, 2010; Kirchengast and Schweitzer, 2011) so that this study is the first one to analyze its performance in a realistic end-to-end simulation framework.

The LMIO observable altitude range focuses on the upper troposphere and stratosphere region (UTLS; ≈ 5 to 35 km). The most important greenhouse gases (GHGs) (CO_2, CH_4, N_2O, H_2O, O_3, CO; incl. key isotopes $^{13}CO_2$, $C^{18}OO$, HDO, $H_2^{18}O$) can be retrieved within an error range of 1 to 3 % r.m.s., while the l.o.s. wind speed is expected to be derivable with good accuracy starting from about 15 up to 35 km, with an expected monthly mean error range of $\pm 1\,m\,s^{-1}$ (Kirchengast and Schweitzer, 2011). Both, GHGs and l.o.s. wind speed, can be retrieved with a vertical resolution of about 1 km.

For the retrieval of GHGs and l.o.s. wind speed the key step is the application of the *differential transmission* concept on an *on-signal* (absorption signal) and *off-signal* (reference signal) in order to essentially eliminate atmospheric broadband effects. In windy air, the IR signal frequencies are influenced by a l.o.s. wind-induced Doppler shift, and as a result the GHG absorption signals (*on-signals*), placed at the center of a target absorption lines under zero wind, are somewhat affected, and therefore also the GHG volume mixing ratio (VMR) retrieval results. The novelty of this study is the complementary implementation of a newly developed l.o.s. wind speed retrieval algorithm (Syndergaard and Kirchengast, 2013) into the overall LMIO algorithm within the eXtended End-to-End Generic Occultation Performance Simulation and Process-

AMTD
8, 405–441, 2015

ing System (xEGOPS), developed at the Wegener Center. Within this framework we can quantitatively assess the l.o.s. wind speed retrieval performance as part of LMIO end-to-end simulations. Furthermore, we can analyze and demonstrate the benefit of a correction of the l.o.s. wind-induced Doppler shift in the IR-laser signal frequencies used for GHG retrievals.

More specifically, the wind retrieval is developed to first determine the l.o.s. wind speed profile from dedicated LIO signals and then feed the GHG retrieval with the estimated wind-induced Doppler shift profile used to correct the nominal zero-wind frequencies of the absorption and reference channels to the actual frequencies applicable in windy air. The purpose is to enable the accurate retrieval of GHGs also in windy air conditions. The wind retrieval uses the assumption of spherically symmetric wind velocities in the atmosphere, a necessary criteria for an Abel transform. A detailed derivation and discussion of the newly developed algorithm itself, and an initial performance assessment under simplified conditions, is provided by Syndergaard and Kirchengast (2013).

Figure 1 shows the LMIO geometry and illustrates MW and IR-laser signal ray paths in windy air conditions. The spherically symmetric wind velocity vectors are indicated with blue arrows. The transmitter (Tx) sends MW and IR-laser signals to a receiver (Rx) while both satellites move in counter-rotating orbits; Kirchengast and Schweitzer (2011) explain the basics in detail. The signals undergo slightly different bending and their ray paths are indicated with different colors; orange for MW and red for IR. The IR-laser signals experience a frequency shift due to relative motion of Tx and Rx, which practically corresponds, for wind speeds of several $10\,\mathrm{m\,s^{-1}}$, to a l.o.s. wind-induced Doppler shift $\Delta f/f$ in the range of 1×10^{-7} at the IR-laser frequencies used for LMIO ($f \approx 143\,\mathrm{THz}$).

The wind retrieval is exploiting this Doppler shift to derive the l.o.s. wind speed. As conceptually introduced by Kirchengast and Schweitzer (2011), this is done by exploiting the Doppler shift-induced delta signal between two differential transmission profiles at the inflection points at the wings of the highly symmetric $C^{18}OO$ absorption line near

AMTD
8, 405–441, 2015

4767 cm^{-1}. This yields a so called *delta-differential transmission profile*, which is found proportional to the prevailing l.o.s. wind speed around the occultation tangent point location via an Abel transform (more details in Sect. 2). For the GHG-targeted absorption signals, which nominally sit at the center of selected GHG absorption lines, this Doppler frequency shift results in the observation of a slightly increased transmission (weaker absorption), since the frequency is shifted off the line center, where maximum absorption would occur.

Here we show the performance of the l.o.s. wind speed retrieval based on the new Abel transform, compared to a simplified previous approach by Schweitzer (2010) and Kirchengast and Schweitzer (2011), and the benefit for the GHG retrieval from correction wind-induced Doppler shift in the GHG channels. We implemented the algorithms in xEGOPS as an add-on to the LMIO algorithm that was introduced and discussed in detail by Proschek et al. (2011); an overview is given in Sect. 2.

We show the LMIO retrieval performance for six representative occultation events, from using a Tx and Rx satellite in near-polar orbits (inclination $\approx 80^{\circ}$) as baselined by Kirchengast and Schweitzer (2011). Two occultation event locations are placed in the tropics, one is at Northern Hemisphere mid-latitudes, one at Southern Hemisphere mid-latitudes, one Northern Hemisphere polar, and one Southern Hemisphere polar, respectively. In this way a diversity of atmospheric conditions is represented over the globe. The six events represent these conditions in terms of thermodynamic profiles (p, T, q) and different l.o.s. wind speed intensities, all extracted from European Centre for Medium-Range Weather Forecasts (ECMWF) analysis fields, for ensuring realistic conditions. The needed GHG profiles for the end-to-end simulations were taken from applicable latitude bands of the Fast Atmospheric Signature Code model (FASCODE, 2008). The forward simulations were done applying spherical symmetry of the atmosphere about tangent point locations and taking the following atmospheric effects into account cf. Schweitzer et al. (2011b): defocusing loss, medium load aerosol extinction, Rayleigh, and scintillations; details on the simulation setup are given in Sect. 3.

AMTD
8, 405–441, 2015

After this introduction the paper is structured as follows. In Sect. 2 we discuss the new l.o.s. wind retrieval algorithm and its implementation integrated within the so-called multi-species retrieval (MSR) part of the LIO retrieval algorithm in xEGOPS. We also discuss the advancement of the GHG retrieval algorithm to account for wind-induced Doppler shift. Next Sect. 3 is presenting the setup for the end-to-end simulations, based on the six representative occultation events mentioned above. Section 4 is then providing the results of the performance analysis both for the new l.o.s. wind retrieval and for the GHG retrieval in windy air. The wind retrieval results discussed relative to previous simplified retrievals, the GHG retrieval with a focus on the VMR results for the representative species CO_2 and H_2O but also showing results for other key species including CH_4 and O_3. Section 5 finally provides a summary and conclusions.

2 Integrating wind profiling into the LIO algorithm

The first detailed description of the LMIO retrieval algorithm in clear air (defocusing loss, Rayleigh scattering, and aerosol extinction) was provided by Proschek et al. (2011). After that the algorithm was updated to add the capability of a GHG retrieval in cloudy air conditions by Proschek et al. (2014). The integration of a proper l.o.s. wind speed retrieval is a next crucial step in the LMIO development taken by this study. Based on the assumption of the wind algorithm that the wind velocity in the occultation plane near the tangent point location is layered in a spherically symmetric way, the retrieval utilizes an Abel transform to calculate the l.o.s. wind speed profile from measured transmission profile data. By applying an Abel transform we are able to accurately retrieve also wind profiles that vary rather strongly with altitude, i.e., we can account also for strong vertical wind shears.

The derivation of an adequate Abel transform providing the relationship between l.o.s. wind speed and the observed (delta-differential) transmission of the two thoroughly chosen wind channels (plus a reference channel) was done in detail by Syndergaard and Kirchengast (2013). Therefore only the resulting key equations are summa-

AMTD
8, 405–441, 2015

rized here. The focus of this section is rather the discussion of the new wind algorithm and its implementation within the MSR part of the xEGOPS simulation software.

The existing GHG retrieval algorithm from LIO is the backbone of the new wind retrieval; a detailed description can be found in Proschek et al. (2011). The dynamic algorithm flow, with the wind profiling inserted, is presented in Fig. 2. The following description can be seen as an update to the algorithm descriptions in Proschek et al. (2011, 2014). Only additional key steps within the overall algorithm and changes in relation to the descriptions in these two publications will be discussed here. The so called simple l.o.s. wind retrieval, which is used for comparison later on in this paper, uses the assumption of a constant l.o.s. wind speed along the entire occultation ray path. This simple retrieval was introduced and described by Schweitzer (2010) and Kirchengast and Schweitzer (2011) and will not be further discussed here.

2.1 The new l.o.s. wind profiling algorithm

All absorption and reference channels which are used within the GHG retrieval are vulnerable to the l.o.s. wind-induced Doppler shift. There are three major contributors to the IR-laser signal's Doppler shift: motion of the Tx and the Rx, Earth's rotation, and the l.o.s. wind speed prevailing in the atmosphere in the occultation plane around the tangent point location. For a frequency $f \approx 143\,\mathrm{THz}$ ($C^{18}OO$ channels near $4767\,\mathrm{cm}^{-1}$) this corresponds to Doppler shifts $\Delta f/f$ of near 2×10^{-5}, 1×10^{-6}, and 1×10^{-7}, respectively (Syndergaard and Kirchengast, 2013). The influence of the motion of the Tx/Rx and of the Earth's rotation can be predicted and accounted for accurately in the instrument design. In particular, these highly predictable kinematic Doppler shifts are foreseen to be compensated on-the-fly in a LMIO mission by adequate Tx frequency design; the recent LMIO mission proposal by Kirchengast et al. (2010) addressed this need.

The remaining Doppler shift caused by the prevailing l.o.s. wind speed is, if not corrected for, adding a small bias to the retrieved GHG profiles in case of wind speeds exceeding $10\,\mathrm{m\,s}^{-1}$ (cf. Schweitzer et al. (2011b), Sect. 3.8.3 therein). On the other

AMTD
8, 405–441, 2015

hand it is this wind-induced Doppler shift that is exploited to derive l.o.s. wind speed profiles from transmission profiles of the wind-sensitive channels near 4767 cm^{-1} at the $C^{18}OO$ absorption line. These Doppler shift estimates are then subsequently used to avoid the bias of the GHG profiles.

Generally it is possible with this method to retrieve l.o.s. wind speeds between about ±1 and ±100 $m\,s^{-1}$ (lower limit from signal-to-noise ratio, upper limit from width of absorption line), which well covers the relevant wind velocities occurring in Earth's troposphere and stratosphere (e.g., Salby, 2012; Plach et al., 2013).

The new l.o.s. wind speed retrieval algorithm starts with the transmission profiles at two wind-sensitive absorption channels (ν_{w1}, ν_{w2}), located at the inflection points of the highly symmetric $C^{18}OO$ absorption line at 4767.041455 cm^{-1} ±0.0004 cm, and the corresponding reference channel at 4770.15 cm^{-1}. Table 1 includes these frequencies. There are some preparatory steps necessary to provide these transmission profiles as a function of impact parameter ("IR impact parameter") and altitude ("IR altitude"), shown in Fig. 2 as gray box. These steps employ existing algorithms, which are discussed in an overview style in Sect. 2.2 below.

The individual wind channel transmission profiles on the IR impact parameter grid and the corresponding reference channel transmission profile are used to derive the differential transmission profiles for the two wind channels, which are then smoothed using a sliding polynomial filter of 3rd order and a filter width of about 1 km. Finally, the so called delta-differential transmission is calculated following

$$\Delta\mathcal{T}(a) = \mathcal{T}_{w1}(a) - \mathcal{T}_{w2}(a), \quad (1)$$

where a denotes the impact parameter and where $\mathcal{T}_{w1}(a)$ and $\mathcal{T}_{w2}(a)$ denote the differential transmissions ($\mathcal{T}_{abs} - \mathcal{T}_{ref}$), respectively, for the two wind channels ν_{w1} and ν_{w2}. Therein, $\mathcal{T}_{abs}$ is the transmission at the absorption channel (*on-line*) and $\mathcal{T}_{ref}$ the transmission at the reference channel (*off-line*). An example for the delta-differential transmission $\Delta\mathcal{T}(a)$ behavior as a function of altitude can be seen in Fig. 2 in the upper right panel, both for constant ±30 $m\,s^{-1}$ wind and for zero wind influence.

AMTD
8, 405–441, 2015

The main equation for the l.o.s. wind speed retrieval via an Abel transform (as a function of the IR impact parameter a) is

$$v(a) \approx \frac{c}{\Delta\chi_0(a)} \left[\frac{1}{\pi} \frac{d}{dr} \int_a^\infty \frac{\Delta\tau(x)dx}{\sqrt{x^2 - a^2}} + \Delta k_0(a) \right] \quad (2)$$

with

$$\Delta\tau(x) = \ln(\Delta\mathcal{T}(a)), \quad (3)$$

and

$$\Delta k_0(a) = k_{w1}(a) - k_{w2}(a), \quad (4)$$

$$\Delta\chi_0(a) = \nu_{w1} \frac{dk_{w1}(a)}{d\nu}|_{\nu_{w1}} - \nu_{w2} \frac{dk_{w2}(a)}{d\nu}|_{\nu_{w2}}. \quad (5)$$

Equations (2), (4), and (5) were derived in Syndergaard and Kirchengast (2013), which contains further details. The main input variables of Eq. (2) are the volume absorption coefficients at the two wind channels $k_{w1}(a)$, $k_{w2}(a)$ (Eq. 4), their spectral derivatives $\frac{dk_{w1}(a)}{d\nu}|_{\nu_{w1}}$, $\frac{dk_{w2}(a)}{d\nu}|_{\nu_{w2}}$ (Eq. 5) and the logarithm of the delta-differential transmission, the delta-differential optical depth $\Delta\tau(x)$ (Eq. 3). Further variables are the speed of light c and the impact parameter a.

Before the $\Delta\mathcal{T}(a)$ and the other key variables can be put into the Abel transform for calculating the l.o.s. wind speed (Eq. 2) a few preparatory steps are necessary. The external Reference Forward Model (RFM) (Edwards, 1996; Dudhia, 2008), a line-by-line radiative transfer model, is called four times to get the volume absorption coefficients $k_{wj\pm h}(a) \pm$ a small increment h displaced from the two wind channels. These values are used to numerically compute a finite-difference estimate of the derivatives $\frac{dk}{d\nu}|_{\nu_{wj}}$ and subsequently compute $\Delta\chi_0(a)$ (Eq. 5). In order to save computational time (by minimizing the number of RFM calls) the values of $k_{wj}(a)$, needed for computing $\Delta k_0(a)$

AMTD
8, 405–441, 2015

(Eq. 4), are obtained by just taking the mean of the two adjacent values at $k_{wj+h}(a)$ and $k_{wj-h}(a)$ ($j = 1,2$ denoting the two wind channels). Sensitivity tests showed that these numerical estimates of the needed variables are very robust and accurate.

Figure 3 illustrates key ingredient variables of the Abel integral, Eq. (2). The left panel is designed to convey the magnitude and the altitude-dependency of the two major inputs of Eq. (2) in addition to $\Delta\tau(x)$, which are $\Delta k_0(a)$ and $\Delta\chi_0(a)$. $\Delta k_0(a)$, the differential volume absorption coefficient between the wind channels (units m^{-1}), shows an exponential dependency and values between about -1×10^{-9} and -1×10^{-13} over 5 to 40 km. $\Delta\chi_0(a)$, the Doppler-shift sensitivity of the volume absorption coefficient (units m^{-1}), on the other hand shows a clear maximum magnitude between 20 and 25 km and ranges between about -0.1 and -1.5 within 5 to 40 km. The right panel of Fig. 3 shows the dependency of the second term in Eq. (2) (units $m\,s^{-1}$), the small "k term" that is added to the Abel integral term. This term again shows an essentially exponential dependency, ranging from about 5 to 5×10^{-5} over 5 to 40 km.

2.2 Greenhouse gas retrieval algorithm under windy air conditions

The GHG retrieval under windy air conditions is an update of the dynamic-loop part of the LMIO algorithm, as introduced above, named Multi-Line Trace Species Retrieval (MSR) loop, which was described in detail by Proschek et al. (2011). Figure 2 illustrates how the modification from wind retrieval insertion comes into the play, integrated with the retrieval of GHGs (and GHG isotopes). We focus on describing this add-on and refer for the basic description to Proschek et al. (2011).

The essential steps for the l.o.s. wind/GHG retrievals happen in the LIO part (red frame). The main input variables of the LIO retrieval are the transmitted LIO signal intensities on the time grid shared with the LMO signals, and the Tx/Rx positions. Furthermore, initial GHG profiles (light green boxes) and an initial l.o.s. wind speed profile (light blue box) on the common altitude (z) grid (shared with LMO parameters) are used as an LIO input.

AMTD
8, 405–441, 2015

The MW impact parameter in combination with the thermodynamic state variables (p,T,q) are used to calculate the needed refractive and geometric IR quantities as preparatory steps (gray box). These preparatory steps are necessary since the needed excess phase observations for deriving these quantities are only accessible in the MW domain but not from the IR intensity-only measurements (IR signal phase tracking would not be robust). The essential IR quantities derived are the IR impact parameter and the IR tangent point altitude. These IR parameters provide an altitude scale, consistent with the LMO data, for the LIO intensity profiles measured as a function of time. This special IR altitude grid estimation is necessary, since the MW and the IR occultation ray paths show (small) differences in bending, which need to be carefully accounted for, especially in the upper troposphere where the humidity is increasing. After the preparatory steps, the new l.o.s. wind speed retrieval component (blue box) is inserted, including the new algorithm after Syndergaard and Kirchengast (2013) as summarized in Sect. 2.1 above.

Next, the Single-Line Trace Species Retrieval (SSR; red box) in Fig. 2 denotes the sequence of steps that are done to perform the retrieval of a single GHG species. The first key step for the present purpose is that differential transmission profiles are derived from each pair of LIO intensity profiles (absorption and corresponding reference channel; see Table 1 for the target species absorption lines and frequencies used) and allocated to the IR altitude grid. Then the differential transmission $\Delta\mathcal{T}(z_i;\nu_j)$ and the modeled species transmission $\Delta\mathcal{T}_{\mathrm{bgr}}(z_i;\nu_j)$ (transmission caused by foreign species; derived from an RFM call with the initial/background GHG profiles) are used to isolate the target species transmission $\Delta\mathcal{T}_{\mathrm{tgt}}(z_i;\nu_j)$ of the absorption channel. In this way the transmission purely due to an individual target GHG becomes known with only negligible influence of foreign species. A so-called *absorptive* Abel transform (Kursinski et al., 2002; Schweitzer et al., 2011b) is then used to derive the target species absorption coefficient on the IR altitude grid. Finally, the target species absorption coefficient and a modeled absorption cross section of the target species (via RFM based on initial/background target species profile and p and T profiles from LMO) are used

AMTD
8, 405–441, 2015

to calculate the retrieved GHG VMR profile. This is the core algorithm. The results are iteratively improved due to subsequent wind and GHG updates, which are explained further down.

The MSR ("inner loop" red box in Fig. 2) is providing a loop to perform a multiple species retrieval in a consecutive, thoroughly defined order over single-line species retrievals (see Table 1 in Proschek et al., 2011). This order ensures that the initial/background GHG profiles are updated so that the SSR can use an improved profile set for every new species retrieval within the MSR loop.

It is possible and useful to perform already the first l.o.s. wind speed retrieval using an initial Doppler shift estimate for the GHG correction of the differential transmission profiles of the two wind channels ($\Delta\mathcal{T}_{w1}, \Delta\mathcal{T}_{w2}$). This Doppler shift estimate can be based on a co-located wind profile from an ECMWF short-range (24 h) forecast field, which we will do in the end-to-end simulations presented in this paper. This approach would also be available for operational processing of real LMIO data and improves the retrieval already at first step (while the same end result after iterations would be reached also for a start with zero wind, i.e., there is no actual a priori dependence). The wind retrieval itself is done as described in the preceding Sect. 2.1.

During the algorithm flow the initial l.o.s. wind speed profile is allocated to the background profile, which after each retrieval is updated with the retrieved l.o.s. wind speed profile between 14 to 45 km wherein the retrieval works well. At the margins of this altitude range there is a smooth transition (half-sine-weighted, 2 km width) to the initial l.o.s. wind speed profile from the ECMWF forecast field, completing the profile below and above for its use for Doppler-shift correction in the GHG retrieval. The altitude range from about 15 to 45 km represents the domain where an accurate l.o.s. wind speed retrieval within the scientific target observational requirements of the LMIO mission concept (Kirchengast et al., 2010) is found possible. The sign of the l.o.s. wind speed is set by the l.o.s. wind direction, which we defined positive if the prevailing wind is blowing towards the Rx.

AMTD
8, 405–441, 2015

The wind correction in the GHG retrieval is implemented as follows. Within the MSR loop, the individual-channel frequency profiles ν_j, originally filled with the nominal frequency ν_0 of the absorption and reference channels, respectively, are adjusted by the Doppler shift induced by the l.o.s. wind speed, $v_{\text{l.o.s.}}$. This frequency profile adjustment, formulated on the altitude grid z_i, reads as follows

$$\nu_{\text{Abs},j}(z_i) = \nu_{\text{Abs},0}(z_i)\left(1 - \frac{v_{\text{l.o.s.}}(z_i)}{c}\right), \tag{6}$$

$$\nu_{\text{Ref},j}(z_i) = \nu_{\text{Ref},0}(z_i)\left(1 - \frac{v_{\text{l.o.s.}}(z_i)}{c}\right), \tag{7}$$

where c is the vacuum speed of light and j serves to index the absorption and reference channel pairs of single GHG species.

Furthermore, the Doppler shift correction is also used to improve the foreign GHG correction in the SSR algorithm (red box in Fig. 2). That is, the frequency shift information is used during the performance of the GHG background correction of the differential transmission profile (cf. Proschek et al., 2011, Sect. 3.4.2 therein), where the target species transmission now in windy air is calculated by

$$\mathcal{T}_{\text{tgt}}(z_i;\nu_j) = \Delta\mathcal{T}(z_i;\nu_j) - \Delta\mathcal{T}_{\text{bgr}}(z_i;\nu_j), \tag{8}$$

where

$$\Delta\mathcal{T}(z_i;\nu_j) = \mathcal{T}_{\text{Abs}}(z_i;\nu_j) - \mathcal{T}_{\text{Ref}}(z_i;\nu_j), \tag{9}$$

and where

$$\Delta\mathcal{T}_{\text{bgr}}(z_i;\nu_j) = \mathcal{T}_{\text{Abs,bgr}}(z_i;\nu_{\text{Abs},j}) - \mathcal{T}_{\text{Ref,bgr}}(z_i;\nu_{\text{Ref},j}). \tag{10}$$

Equations (8) to (10) are updated from Proschek et al. (2011) (Eqs. 13 to 15 therein). From $\Delta\mathcal{T}_{\text{tgt}}(z_i;\nu_j)$ onwards the algorithm again follows the clear air algorithm as described in Proschek et al. (2011) (cf. Fig. 2 with Fig. 2 in Proschek et al., 2011).

AMTD
8, 405–441, 2015

The l.o.s. wind-corrected frequencies are applied for each GHG species within the MSR loop so that the background GHG profiles are updated with retrieved GHG profiles that are already corrected for l.o.s. wind-induced Doppler shift. After the inner loop is finished first-time the basic run of the MSR loop is completed for all GHG species.

After this basic run, the so-called outer loop (Basic-Update-Control (BUC) loop) is initiated. It takes the GHG and l.o.s. wind output profiles and feeds them again, as new background profiles, into the algorithm. In this way the l.o.s. wind speed retrieval is further improved again during the update run, and subsequently also the GHG retrieval during the update MSR loop. Another complete run, the control run that uses the outputs of the update run as input, finally ensures and controls the convergence of the l.o.s. wind speed and GHG results; its results nominally have negligible deviation from the results of the update run as demonstrated by Proschek et al. (2011).

3 End-to-end simulation setup

We performed LMIO end-to-end simulations with the eXtended End-to-End Generic Occultation Performance Simulation and Processing System (xEGOPS)/End-to-End Generic Occultation Performance Simulation and Processing System (EGOPS) using realistic atmospheric conditions for MW and IR-laser signals. The xEGOPS system is a development environment based on the operational EGOPS system, which performs the LMO end-to-end simulations. xEGOPS adds the LIO end-to-end simulations, using the EGOPS kernel library, and is designed to enable the integration of such new algorithms under development (Fritzer et al., 2009, 2010).

In this section we discuss the setup of the simulations and the atmospheric thermodynamic, wind, and GHG conditions. The first step of the end-to-end simulations is the calculation of geometric orbit arcs of the Tx and Rx satellites and of the geometric tangent point locations for every occultation event. These calculations were done with the Mission Analysis/Planing (MAP) sub-tool of the EGOPS/xEGOPS system. We used near-polar orbits with an inclination of $\approx 80^{\circ}$, in line with the ACCURATE mission con-

AMTD
8, 405–441, 2015

cept proposal of Kirchengast et al. (2010). Based on the occultation event simulations of a full day, six representative example events were selected to represent different atmospheric conditions. The global distribution of the occultation events is illustrated in Fig. 4.

The next step of simulation is the propagation of the MW and the IR-laser signals through the atmosphere, which was carried out with the Forward Modelling (FOM) sub-tool of the EGOPS/xEGOPS system. We use an elliptical Earth figure model (World Geodetic System 1984 (WGS84)), spherical symmetry of the atmosphere at the occultation event locations, and a sampling rate of 10 Hz. Both the MW and IR-laser signals undergo refraction, defocusing, and absorption loss (Kursinski et al., 2000). The IR-laser signals were treated to be additionally influenced by aerosol extinction (medium aerosol load), Rayleigh scattering, and scintillations (Schweitzer et al., 2011b).

We calculate the IR absorption with the RFM model, employing the High Resolution Transmission (HITRAN) 2008 (Rothman et al., 2009) database for supplying the spectroscopic line parameters. Table 1 summarizes the wavenumbers used for the absorption and reference channels, plus the corresponding frequency spacing. The representative GHG concentrations for the simulations of the molecular absorption were taken from the FASCODE atmosphere. This RFM/HITRAN/FASCODE subsystem is integrated in the FOM sub-tool of the EGOPS/xEGOPS system so that realistic IR absorption computations along ray propagation paths are seamlessly possible.

The used HITRAN 2008 version includes a pressure shift parameter for the $C^{18}OO$ absorption line. This introduces an altitude dependency to the absorption frequencies. It would have been a special effort to implement the frequencies as vectors within xEGOPS to take this dependency into account, which are currently implemented as scalars. We therefore disregarded the pressure shift parameter for the $C^{18}OO$ line in the present simulations, also reflecting that the actual system would compensate for the wind-line pressure shift by its tunable Tx frequency design. We note also that the study by Syndergaard and Kirchengast (2013) showed that the Δk_0 term in the Abel transform compensates for the pressure shift within the retrieval if it is not corrected.

AMTD
8, 405–441, 2015

Thus ignoring the pressure shift in the simulations is a reasonable choice not limiting the realistic character of the results obtained. For all other IR-laser channels for the GHG retrieval pressure shift is included if HITRAN 2008 includes this information for the target absorption lines.

To further increase the realism of the simulations, an LIO scintillation model is included within the FOM sub-tool. The scintillation fluctuations are superimposed on the forward-modeled signals. This ensures that the influence of atmospheric turbulence, causing scintillations in LIO signals, is appropriately considered. The model is based on scintillation data from the GOMOS (Global Ozone Monitoring by Occultation of Stars) instrument (Sofieva et al., 2009) and was developed by Sofieva et al. (2009) following the theoretical analyses of Horwath and Perlot (2008). The model is build on stratified altitude-dependent scintillations that saturate below about 20 km. This is in agreement with GOMOS observations and experimental results by Gurvich et al. (1996).

Individual signals of single frequency channels are strongly influenced by turbulence as discussed by Schweitzer et al. (2011a). Although scintillations do fairly quickly decorrelate over frequency, the narrow spacing of absorption and reference channel of < 0.1 % for the two wind channels (see Table 1) results in a very small influence of scintillations. For further details on scintillations see also Schweitzer et al. (2011a).

Following the FOM step, the influence of the observation system is modeled, employing the EGOPS/xEGOPS-Observation System Modelling (OSM) sub-tool. In this process, the OSM is superimposing observational errors on the FOM signals, which have included only the effects of atmospheric propagation. The OSM adds Precise Orbit Determination (POD) errors, thermal noise errors, intensity drift, and clock errors in the same way as Proschek et al. (2011) did, where a more detailed description of the modeling of the OSM errors is provided.

To complete the end-to-end simulations, the retrieval is performed with the Occultation Processing System (OPS) sub-tool of the EGOPS/xEGOPS software. The thermodynamic state variables, including temperature, pressure, and humidity, are obtained from the LMO-based MW retrieval of EGOPS (Schweitzer et al., 2011b). These vari-

AMTD
8, 405–441, 2015

ables, in combination with the altitude level information, are the basis for the LIO-based IR retrieval of xEGOPS (Proschek et al., 2011). The new l.o.s. wind speed retrieval, and the GHG retrieval including correction of wind-induced Doppler shift, is embedded within the LIO retrieval algorithm as described in Sect. 2 above.

The influence of the l.o.s. wind on the GHG retrieval is investigated at six geographical locations, representing a good diversity of atmospheric conditions: a warm and moist tropical atmosphere – Tropical (TRO-1/2), a standard mid-latitude atmosphere – Northern Hemisphere mid-latitudes (NHM) and Southern Hemisphere mid-latitudes (SHM), and a cold and dry sub(ant)arctic winter atmosphere – Northern Hemisphere polar (NHP) and Southern Hemisphere polar (SHP).

In order to demonstrate the capability of the new l.o.s. wind retrieval and of the GHG algorithm under windy air conditions, the locations were chosen to include both high-end wind velocities (especially represented by the polar cases) and quite variable vertical wind shear (especially represented by the tropical cases). The atmospheric thermodynamic and wind variables at the occultation event locations were extracted from ECMWF atmospheric fields, where we used an analysis field for providing "true" profiles to the FOM, and a short-range forecast field for providing initial/background profiles to the OPS.

The global distribution of the example occultation events for 15 July 2007, obtained with the near-polar satellite orbits (inclination $\approx 80^{\circ}$), is shown in Fig. 4. The six selected occultation events are highlighted with colors according to their latitude. The ECMWF fields were used for the same day (15 July 2007, 12:00 UTC time layer).

Figure 5 presents the atmospheric conditions at the six occultation event locations. In the left column the temperature (T) profiles for the six locations are shown. The middle column presents the "true" l.o.s. wind speed ($v_{\text{l.o.s.}}$) profiles and the right column the corresponding delta-differential transmission ($\Delta\mathcal{T}$) profiles. The T and $v_{\text{l.o.s.}}$ profiles are as used in the FOM, and the $\Delta\mathcal{T}$ profiles as obtained in the OPS as key input to the *wind* Abel transform (Eq. 2).

AMTD
8, 405–441, 2015

As seen in Fig. 5, the cases represent a good variety of different thermodynamic and windy air situations, including winds ranging from weak to strong wind speeds and from weak to strong vertical wind shears. The TRO-1/2 cases (top row, red profiles) show a sharp tropopause, rather weak but vertically highly variable winds, and as a result also weak $\Delta\mathcal{T}$ signals. The NHM and SHM cases (middle row, green profiles) exhibit more disturbed T profiles, already somewhat stronger winds, and higher overall wind shear especially in the NHM case. The strongest l.o.s. wind speeds can be seen for the SHP case (bottom row, dark-blue profile), with values exceeding 70 m s^{-1} in the upper stratosphere, while a rather calm wind prevails in the NHP case. Therefore the SHP case also shows the strongest $\Delta\mathcal{T}$ signal.

4 Demonstration results

Here we present results of the the LMIO end-to-end simulations under windy air conditions according to the setup above, in order to demonstrate the performance of the advanced retrieval. We start with a comparison of the new Abel transform-based wind retrieval with the previously introduced simple wind retrieval (Schweitzer, 2010; Kirchengast and Schweitzer, 2011).

Figure 6 shows the comparison of the new and the simple l.o.s. wind retrieval for the TRO-1 and SHP example cases, which are neatly representing quite different conditions. The "true" l.o.s. wind speed profile is shown for reference. The SHP case shows high l.o.s. wind speeds up to 75 m s^{-1}, while the TRO-1 case shows comparatively small l.o.s. wind speeds but with higher wind shears. The new wind retrieval results are in very good agreement with the "true wind" over about 15 to 35 km, both for weak and very strong wind speeds, while the simple wind retrieval results show major deviations and overly strict vertical smoothing at all altitude levels. This confirms the expectations of Schweitzer (2010) and Kirchengast and Schweitzer (2011) who argued that the formulation of an Abel transform-type retrieval algorithm, as then formulated by Syn-

AMTD
8, 405–441, 2015

dergaard and Kirchengast (2013), should markedly improve the retrieval performance compared to the simple retrieval approach.

Figure 7 presents the l.o.s. wind speed error in form of a small-ensemble statistics result from all six cases. This result very clearly shows the superiority of the new wind retrieval (left panel) over the simple wind retrieval (right panel) both in avoiding biased retrieval and in reducing the r.m.s. error. The Abel transfrom-based retrieval is capable to achieve the scientific target requirements of $2\,m\,s^{-1}$ r.m.s. error over most of the target domain from 15 to 35 km and retrieves within 5 up to 40 km. Below about 15 km the retrieval quality rapidly degrades due to the decreasing signal-to-noise ratio for the delta-differential transmission signals.

Building on the favorable performance of the Abel transform-based wind retrieval, Fig. 8 demonstrates the influences of the correction of wind-induced Doppler shift on the GHG retrieval, again by using the two representative TRO-1 (left) and SHP (right) example cases. The GHG example species are CO_2 (top) and H_2O (bottom), both representing quite different LIO trace species retrieval challenges as seen by the studies of Proschek et al. (2011) and Proschek et al. (2014). VMR errors are shown and the retrieval results without Doppler shift correction (i.e., ignoring the windy air and assuming zero wind) are shown as gray profiles for reference. Overall we see that the VMR retrieval errors with the Doppler shift correction, and in case of sufficiently weak wind also without, basically appear to stay in an r.m.s. sense within the scientific target requirements of 2 % for CO_2 and 4 % for H_2O.

Looking specifically at the TRO-1 case, it is clear that the Doppler shift correction shows only a very minor influence (the red profiles essentially shadow the gray profiles), since the l.o.s. wind speed at this tropical location is rather low (within $\pm 10\,m\,s^{-1}$; see Fig. 5). This confirms the initial simple estimates of Schweitzer et al. (2011b) that wind speeds not exceeding $10\,m\,s^{-1}$, or where the uncertainty of wind profiles used for the correction would not exceed this level, are not critical to the accuracy of the GHG retrievals. At the SHP location, with much higher l.o.s. wind speeds up to $\approx 75\,m\,s^{-1}$ in the upper stratosphere (see Fig. 5), the influence of the correction is well visible,

AMTD
8, 405–441, 2015

however. It provides for a clear improvement in this case, eliminating biased retrieval over the stratosphere. Here in particular the CO_2 retrieval is more sensitive than the H_2O retrieval, due to somewhat different lineshapes of the corresponding absorption lines.

One general conclusion here is as well that for aiding the GHG retrieval with Doppler shift correction also ECMWF short-range forecast wind fields can generally do a reasonable job given their wind uncertainties typically do not exceed 10 m s^{-1}. For climate monitoring purposes a self-consistent solution with joint wind and GHG retrieval from LMIO data is nevertheless preferable.

Figure 9 shows the VMR retrieval errors, including Doppler shift correction under the given windy air conditions, for the GHG species CO_2 (upper left), CH_4 (upper right), H_2O (lower left) and O_3 (lower right) in form of a small-ensemble statistics result from all six selected occultation events. This serves to illustrate the overall performance achievable for different key species. The results for all species are essentially unbiased, which is very encouraging for LMIO implementation, since it is one core promise to qualify as a climate benchmark dataset.

The CO_2 and H_2O stay within scientific target requirements over most of the vertical domain, as already indicated in the single-profile results of Fig. 8. The CH_4 results stay within requirements up to about 25 km, above which the CH_4 VMR becomes small and the signal-to-noise ratio degrades primarily due to residual scintillation noise, which governs the noise budget at these altitudes.

Finally, the O_3 results are within the requirements over the stratospheric ozone layer down to about 20 to 15 km, where the downward increase of errors strongly depends on whether tropical cases with very low (tropospheric) ozone concentrations up to about 18 km are involved or not, since the extratropical air is richer in ozone lower down. Compared to the earlier O_3 retrieval performance results of Proschek et al. (2011), these O_3 results also reflect that the new O_3 channel selections (near 4670 cm^{-1} rather than near 4030 cm^{-1} as originally selected by Kirchengast and Schweitzer (2011); see

AMTD
8, 405–441, 2015

Table 1) exhibit somewhat less absorber sensitivity (but are technically much more convenient to implement together with all other channels).

5 Summary and conclusions

We introduced an advanced l.o.s. wind speed retrieval, based on a new *wind* Abel transform Syndergaard and Kirchengast (2013), into the existing LMIO algorithm described by (Proschek et al., 2011). Making use of this new wind retrieval we also integrated a correction for wind-induced Doppler shift into the GHG retrieval algorithm, which might otherwise lead to slightly biased retrievals under windy air conditions.

We described the new l.o.s. wind speed retrieval and the Doppler shift correction in the GHG retrieval and evaluated the performance of the advanced LMIO algorithm based on realistic end-to-end simulations for six representative occultation events spanning a good diversity of atmospheric conditions from tropical to high-latitude winter. The retrieval was performed for the thermodynamic state variables temperature, pressure and humidity from the microwave channels, for the l.o.s. wind speed from the two IR-laser wind channels at the highly symmetric $C^{18}OO$ absorption line. The GHG retrievals from IR-laser channels were performed for the representive species CO_2, CH_4, H_2O, and O_3.

For assessing the performance of the new Abel transform wind retrieval it was compared to the initial simple wind retrieval approach of Schweitzer (2010) and Kirchengast and Schweitzer (2011). This showed significant benefit and improvement from the new Abel transform retrieval, since it can account for the spherical symmetry of the problem while the simple wind retrieval strongly over-smoothes vertical wind variations.

The results for the six example occultation events showed the reliability of the Abel transform retrieval for providing l.o.s. wind speeds in an essentially unbiased manner and generally with errors within the target requirment range of $2\,m\,s^{-1}$, throughout the lower stratosphere over about 15 to 35 km. Below 15 km the retrieval errors increase rapidly due to the decreasing signal-to-noise ratio of the delta-differential transmission

AMTD
8, 405–441, 2015

observable. The simple wind retrieval is not capable to reliably derive realistic l.o.s. winds within scientific observation requirements. This underscores the importance of the new Abel transform for enabling accurate wind profiling based on IR-laser occultation data also in windy air including under strong winds conditions.

The correction of the wind-induced Doppler shift influence in the GHG retrieval shows significant benefit for the GHG retrieval results, in particular in case of strong winds. Weak l.o.s. winds with speeds not exceeding $10\,m\,s^{-1}$ have no appreciable influence on the GHG results, as anticipated by Schweitzer et al. (2011a) based on preliminary estimates. This is favorable since it implies that winds need not be known more accurate than about $10\,m\,s^{-1}$ for the purpose of supporting GHG retrieval. This also justifies the use of co-located winds from ECMWF analysis or short-range forecast fields in the troposphere below 15 km, where the retrieved winds are of lower quality.

The GHG retrieval results in windy air were found promising, since all retrieved species (CO_2, CH_4, H_2O, and O_3) were found essentially unbiased and generally within the scientific target requirement ranges of 2 to 4 % over the upper troposphere and lower stratosphere. CO_2 and H_2O are of very coherent quality throughout this range. CH_4 errors increase above about 25 km and O_3 errors below about 20 to 15 km, both due to decreasing signal-to-noise ratio in these upper/lower domains, where the noise is dominated by residual scintillation noise as also found by Proschek et al. (2014).

Overall the new Abel transform wind retrieval is found to enable accurate stratospheric wind profiling based on IR-laser occultation data in windy air, including under strong wind conditions and under variable vertical wind shears. The GHG retrieval including correction for the l.o.s. wind-induced Doppler shift as well shows robust and accurate retrieval results under all windy air conditions and therefore enables benchmark-quality greenhouse gas profiling also in windy air. These results are encouraging towards further development and implementation of an LMIO mission.

Acknowledgements. We thank S. Syndergaard (DMI, DK) for valuable discussions on the application of the wind Abel transform and for the excellent collaboration in its development. EGOPS was developed by an international consortium led by UniGraz (AT) and involving partners at

AMTD
8, 405–441, 2015

Danish Meteorol. Inst. (DK), Obukhov Inst. of Atmos. Physics (RU), Chalmers Univ. of Technology (SE), Univ. of Bremen (DE), Met. Office (UK), Terma Elektronik A/S (DK), and RUAG Space GmbH (AT). xEGOPS was developed by UniGraz (AT), with contributions by E. Martini (CNIT, IT) and V. Sofieva (FMI, FI) to scintillation modeling and by C. Emde (Univ. of Munich, DE) to cloud extinction modeling. Funds for the EGOPS/xEGOPS development were provided by ESA/ESTEC (NL), FWF and FFG-ALR (AT), and EUMETSAT/HQ (DE). Access to atmospheric analysis fields was provided by the ECMWF, access to RFM and FASCODE by A. Dudhia (Univ. of Oxford, UK) via www.atm.ox.ac.uk/RFM, and access to HITRAN by L. Rothman (Harvard Univ., USA) via www.cfa.harvard.edu/hitran. This work was funded by ESA under the AEXPWIND project (ESA/ESTEC Contract No. 4000105679/12/NL/CBi).

References

Andrews, L. C. and Philips, R. L.: Laser Beam Propagation Through Random Media, 2nd edn., SPIE Press, Bellingham, Washington, USA, 2005. 408

Dudhia, A.: Reference Forward Model RFM: Inst. of Atmos., Oceanic and Planet. Phys., Univ. of Oxford, Oxford, UK, available at: http://www.atm.ox.ac.uk/RFM/ (last access: 31 October 2014), 2008. 414

Edwards, D. P.: High level algorithm definition document, Tech. Rep. ESA/ESTEC PO-TN-OXF-GS-0004, Contract No. 11886/96/NL/GS, Inst. of Atmos., Oceanic and Planet. Phys., Univ. of Oxford, Oxford, United Kingdom, available at: http://www.atm.ox.ac.uk/RFM/ (last access: 31 October 2014), 1996. 414

FASCODE: cited 2008 on RFM website – FASCODE model atmospheres: Inst. of Atmos., Oceanic and Planet. Phys., Univ. of Oxford, Oxford, UK, available at: http://www.atm.ox.ac.uk/RFM/atm (last access: 31 October 2014), 2008. 410

Fritzer, J. M., Kirchengast, G., and Pock, M.: End-to-End Generic Occultation Performance Simulation and Processing System Version 5.5 – Detailed Design Document, Tech. Rep. for ESA-ESTEC No. 2/2009, Wegener Center and Inst. for Geophys., Astrophys., and Meteorol., Univ. of Graz, Graz, Austria, 2009. 419

Fritzer, J. M., Kirchengast, G., Pock, M., and Proschek, V.: End-to-End Generic Occultation Performance Simulation and Processing System Version 5.5 (EGOPS 5.5 and xEGOPS) –

AMTD
8, 405–441, 2015

Detailed Design Document, Tech. Rep. for ESA-ESTEC No. 2/2010, Wegener Center and Inst. for Geophys., Astrophys., and Meteorol., Univ. of Graz, Graz, Austria, 2010. 419

Gurvich, A. S., Kan, V., and Fedorova, O. V.: Refraction angle fluctuations in the atmosphere from space observations of stellar scintillations, Atmospheric and Oceanic Physics, 31, 742–749, englisch version, 1996. 421

Gurvich, A. S., Gorbunov, M. E., Fedorova, O. V., Kirchengast, G., Proschek, V., González Abad, G., and Tereszchuk, K. A.: Spatiotemporal structure of a laser beam over 144 km in a Canary Islands experiment, Appl. Optics, 51, 7374–7383, doi:10.1364/AO.51.007374, 2012. 408

Horwath, J. and Perlot, N.: Atmospheric impacts on ILO signals: Scintillation, Tech. Rep. for ESA-ESTEC Technical Note 4 – Part of the TR-IRPERF Report, DLR Oberpfaffenhofen, Oberpfaffenhofen, Germany, 2008. 421

Kirchengast, G. and Schweitzer, S.: Climate benchmark profiling of greenhouse gases and thermodynamic structure and wind from space, Geophys. Res. Lett., 38, L13701, doi:10.1029/2011GL047617, 2011. 407, 408, 409, 410, 412, 423, 425, 426

Kirchengast, G., Bernath, P. F., Buehler, S., Durry, G., Facheris, L., Gerbig, C., Haimberger, L., Harris, J., Hauchecorne, A., Kurölä, E., Larsen, G. B., Sausen, R., Anthes, R. A., Gorbunov, M. E., Kursinski, E. R., Leroy, S. S., Trenberth, K., Randel, B., Gille, J., and Tsuda, T.: ACCURATE – climate benchmark profiling of greeenhouse gases and thermodynamic variables and wind from space (ESA Earth Explorer Opportunity Mission EE-8 proposal), Sci. Rep. No. 36, document wcv-scirep-no36-gkirchengastetal-jul2010.pdf, Wegener Center Verlag, Graz, Austria, available at: http://www.wegcenter.at/wcv (last access: 31 October 2014), 2010. 407, 412, 417, 420

Kursinski, E. R., Hajj, G. A., Schofield, J. T., Linfield, R. P., and Hardy, K. R.: Observing Earth's atmosphere with radio occultation measurements using the global positioning system, J. Geophys. Res.-Atmos., 102, 23429–23465, 1997. 407

Kursinski, E. R., Hajj, G. A., Leroy, S. S., and Herman, B.: The GPS radio occultation technique, Terr. Atmos. Ocean. Sci., 11, 53–114, 2000. 407, 420

Kursinski, E. R., Syndergaard, S., Flittner, D., Feng, D., Hajj, G., Herman, B., Ward, D., and Yunck, T.: A microwave occultation observing system optimized to characterize atmospheric water, temperature and geopotential via absorption, J. Atmos. Ocean. Tech., 19, 1897–1914, doi:10.1175/1520-0426(2002)019<1897:AMOOSO>2.0.CO;2, 2002. 416

AMTD
8, 405–441, 2015

Liou, K. N.: An Introduction to Atmospheric Radiation, Academic Press, San Diego, California, USA, 2nd edn., 2002. 407

Plach, A., Proschek, V., and Kirchengast, G.: Abel transform retrieval of wind profiles from LEO-LEO IR laser occultation: End-to-end simulations and performance analysis, Tech. Rep. ESA-ESTEC-2/2013 (AEXPWIND TN3 – Part2), Wegener Center, Univ. of Graz, Graz, Austria, 2013. 413

Proschek, V., Kirchengast, G., and Schweitzer, S.: Greenhouse gas profiling by infrared-laser and microwave occultation: retrieval algorithm and demonstration results from end-to-end simulations, Atmos. Meas. Tech., 4, 2035–2058, doi:10.5194/amt-4-2035-2011, 2011. 407, 408, 410, 411, 412, 415, 417, 418, 419, 421, 422, 424, 425, 426, 434

Proschek, V., Kirchengast, G., Emde, C., and Schweitzer, S.: Greenhouse gas profiling by infrared-laser and microwave occultation in cloudy air: results from end-to-end simulations, J. Geophys. Res. Atmos., 119, 12372–12390, doi:10.1002/2014JD021938, 2014. 407, 408, 411, 412, 424, 427

Rothman, L. S., Gordon, I. E., Barbe, A., Benner, D. C., Bernath, P. F., Birk, M., Boudon, V., Brown, L. R., Campargue, A., Champion, J.-P., Chance, K., Coudert, L. H., Dana, V., Devi, V. M., Fally, S., Flaud, J.-M., Gamache, R. R., Goldman, A., Jacquemart, D., Kleiner, I., Lacome, N., Lafferty, W. J., Mandin, J.-Y., Massie, S. T., Mikhailenko, S. N., Miller, C. E., Moazzen-Ahmadi, N., Naumenko, O. V., Nikitin, A. V., Orphal, J., Perevalov, V. I., Perrin, A., Predoi-Cross, A., Rinsland, C. P., Rotger, M., Šimečková, M., Smith, M. A. H., Sung, K., Tashkun, S. A., Tennyson, J., Toth, R. A., Vandaele, A. C., and Vander Auwera, J.: The HITRAN 2008 molecular spectroscopic database, J. Quant. Spectrosc. Ra., 110, 533–572, doi:10.1016/j.jqsrt.2009.02.013, 2009. 420

Salby, M. L.: Fundamentals of Atmospheric Physics, vol. 61, Academic Press, San Diego, 1996. 407

Salby, M. L.: Physics of the Atmosphere and Climate, Cambridge University Press, New York, 2012. 407, 413

Schweitzer, S.: The ACCURATE concept and the infrared laser occultation technique: Mission design and assessment of retrieval performacne (Ph. D. thesis), Sci. Rep. No. 34, document wcv-scirep-no34-sschweitzer-jun2010.pdf, Wegener Center Verlag, Graz, Austria, available at: http://www.wegcenter.at/wcv (last access: 31 October 2014), 2010. 407, 408, 410, 412, 423, 426

AMTD
8, 405–441, 2015

Schweitzer, S., Kirchengast, G., and Proschek, V.: Atmospheric influences on infrared-laser signals used for occultation measurements between Low Earth Orbit satellites, Atmos. Meas. Tech., 4, 2273–2292, doi:10.5194/amt-4-2273-2011, 2011a. 407, 421, 427

Schweitzer, S., Kirchengast, G., Schwärz, M., Fritzer, J. M., and Gorbunov, M. E.: Thermodynamic state retrieval from microwave occultation data and performance analysis based on end-to-end simulations, J. Geophys. Res. Atmos., 116, D10301, doi:10.1029/2010JD014850, 2011b. 407, 408, 410, 412, 416, 420, 421, 424

Sofieva, V. F., Kan, V., Dalaudier, F., Kyrölä, E., Tamminen, J., Bertaux, J.-L., Hauchecorne, A., Fussen, D., and Vanhellemont, F.: Influence of scintillation on quality of ozone monitoring by GOMOS, Atmos. Chem. Phys., 9, 9197–9207, doi:10.5194/acp-9-9197-2009, 2009. 421

Syndergaard, S. and Kirchengast, G.: Formulation and analysis of an Abel transform for deriving line-of-sight wind profiles from LEO-LEO IR laser occulation, Tech. Rep. ESA-ESTEC-1/2013 (AEXPWIND TN3 – Part1), Wegener Center, Univ. of Graz, Graz, Austria, 2013. 408, 409, 411, 412, 414, 416, 420, 423, 426

Ware, R., Exner, M., Feng, D., Gorbunov, M. E., Hardy, K., Herman, B. M., Kuo, W., Meehan, T., Melbourne, W., Rocken, C., Schreiner, W., Sokolovskiy, S., Solheim, F., Zou, X., Anthes, R., Businger, S., and Trenberth, K.: GPS sounding of the atmosphere from low Earth orbit: preliminary results, B. Am. Meteorol. Soc., 77, 19–40, 1996. 407

AMTD
8, 405–441, 2015

Table 1. Infrared-laser absorption and reference channels used for the study (wavenumber data based on HITRAN 2008).

Target species	Absorption wavenumber cm^{-1}	Reference wavenumber cm^{-1}	(Abs.-Ref.)/Ref. freq. spacing %
$C^{18}OO$-w1	4767.037455	4770.15	−0.0653
$C^{18}OO$-w2	4767.045455	4770.15	−0.0651
$^{12}CO_2$	4771.621441	4770.15	+0.0308
$^{13}CO_2$	4723.414985	4731.03	+0.1610
CH_4	4344.163500	4322.93	+0.4912
H_2O-1	4204.840290	4227.07	−0.5259
H_2O-2	4775.802970	4770.15	+0.1185
H_2O-3	4747.054840	4731.03	+0.3387
H_2O-4	4733.045010	4731.03	+0.0426
O_3	4667.115600	4670.17	+0.0655

AMTD
8, 405–441, 2015

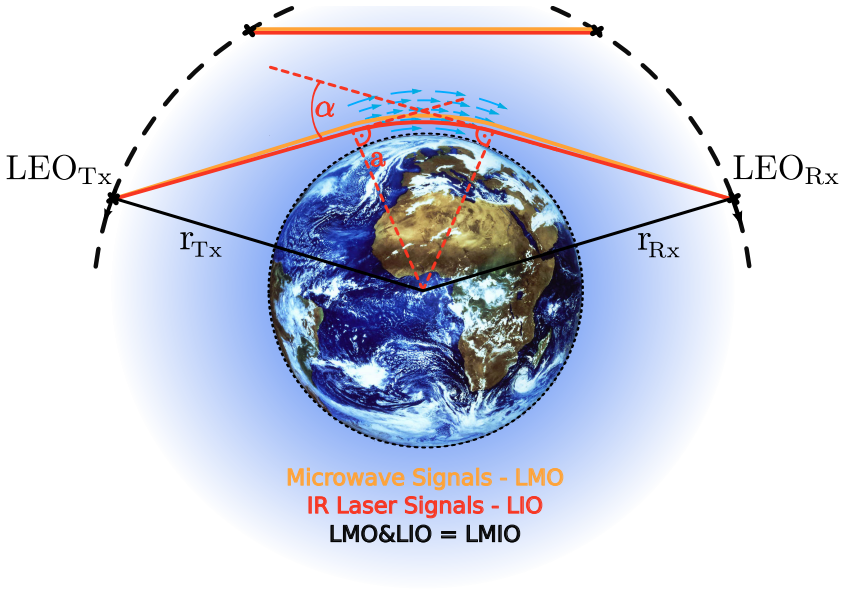

Figure 1. Schematic overview of the LMIO geometry and setup. The blue arrows symbolize the spherically symmetric l.o.s. wind. Tx and Rx are the transmitter and receiver instruments on the LEO satellites. r_{Tx} and r_{Rx} are the radial distances from the Tx and Rx to the center of curvature of the Earth. α denotes the bending angle of the IR signal, shown as a function of impact parameters a.

AMTD
8, 405–441, 2015

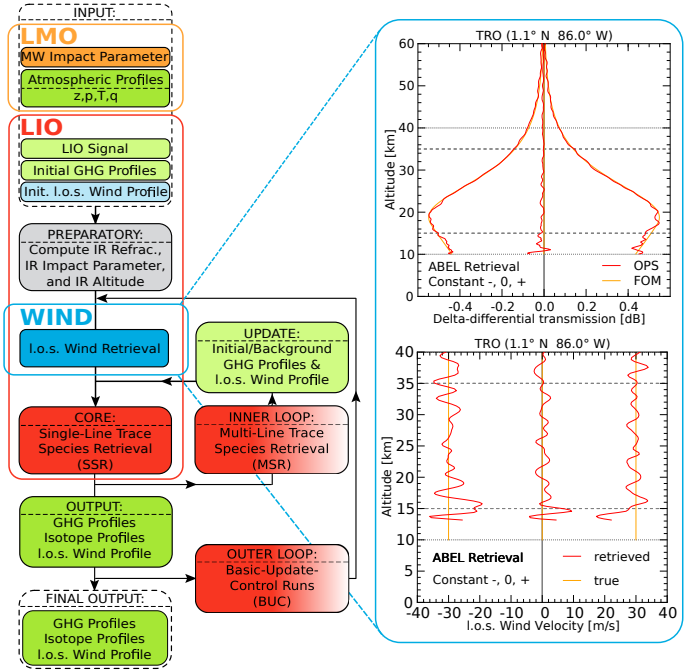

Figure 2. Schematic overview of the dynamical LIO wind and GHG retrieval algorithm, comprising the input parameters from LMO (orange framed box) and LIO (together with LMO the dashed-black framed box), and for the LIO retrieval the preparatory steps (grey box), the wind retrieval step (blue box, plus exemplary delta-differential transmission and resulting wind profiles illustrated as "flyout graphics" at the right hand side), and the core algorithm (SSR; red box). The GHG retrieval inner loop (MSR; red gradient box), computing and updating (light-green box) the GHGs in a pre-defined appropriate order, and the outer loop (basic-update-control runs; lower red gradient box), leading at the end to the final output (bottom green box), are sketched as well. Figure updated from Proschek et al. (2011).

AMTD
8, 405–441, 2015

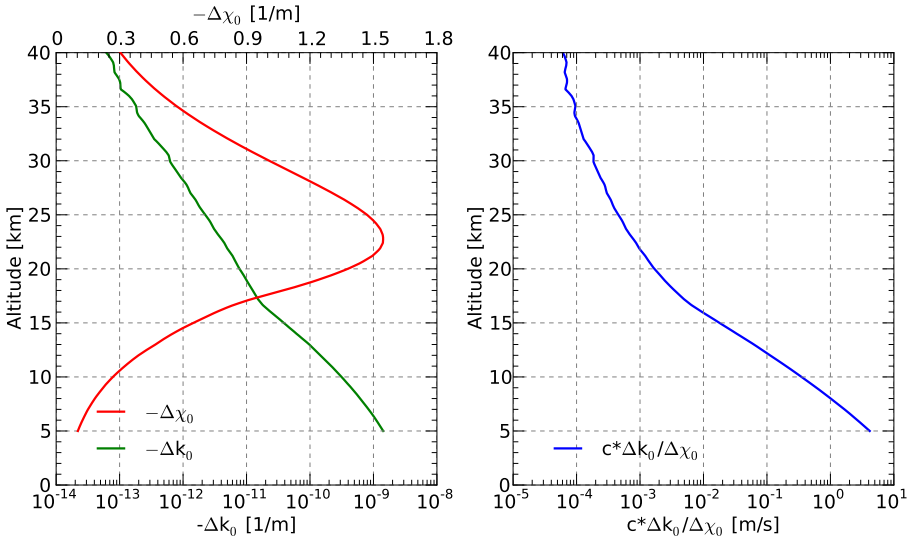

Figure 3. Left: Profiles of two key input variables into the new Abel transform for the l.o.s. wind profiling. Δk_0 is a differential volume absorption coefficient between the wind channels and $\Delta\chi_0$ an associated differential absorption coefficient derivative. Right: Profile of the "k term", which appears as the small second term in the wind Abel transform (Eq. 2).

AMTD
8, 405–441, 2015

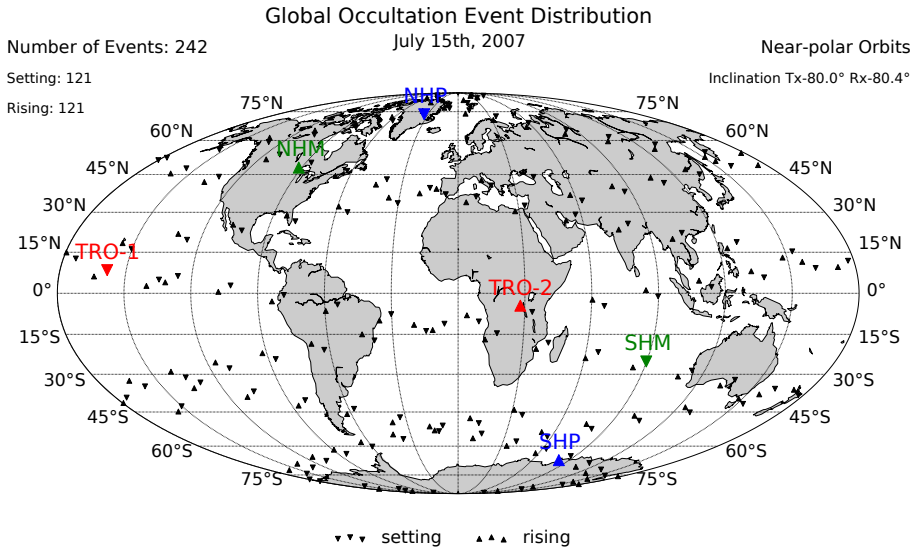

Figure 4. Global distribution of the occultation events on 15 July 2007 using near-polar ($i \approx 80^{\circ}$) orbits. Rising events are indicated with upright triangles, while setting events are represented using reversed (upside-down) triangles. The six occultation event locations used for the study are colored in red, green and blue according to their latitude band.

AMTD
8, 405–441, 2015

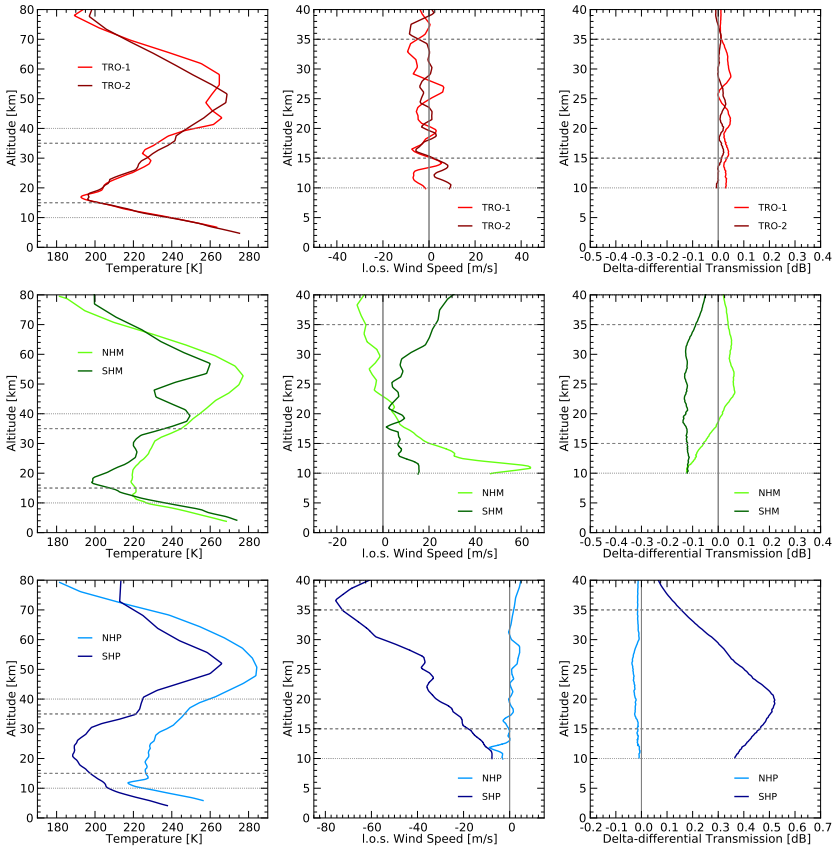

Figure 5. Temperature profiles (left), l.o.s. wind speed profiles (middle), and delta-differential transmission profiles (right) of the six selected atmospheric cases. The top row (red profiles) shows the TRO-1/2 cases, while the middle one (green profiles) shows the NHM and SHM cases and the bottom one (blue profiles) the NHP and SHP cases, respectively.

AMTD
8, 405–441, 2015

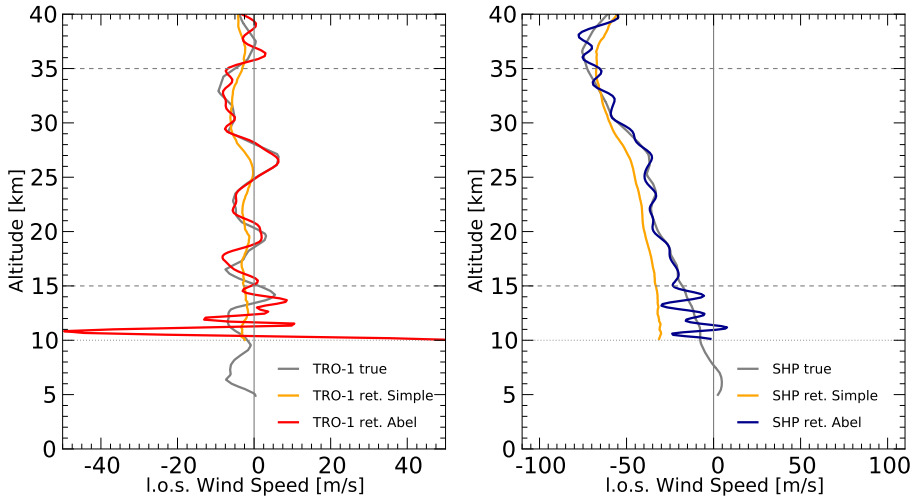

Figure 6. Abel transform and simple retrieval results for two representative cases. Left: simple retrieval (orange) and Abel transform retrieval (red) l.o.s. wind speed for the TRO-1 case (red line). Right: simple retrieval (orange) and Abel transform retrieval (blue) results for the SHP case. The gray profile is, in both panels, the "true" profile used in the forward modeling of the events.

AMTD
8, 405–441, 2015

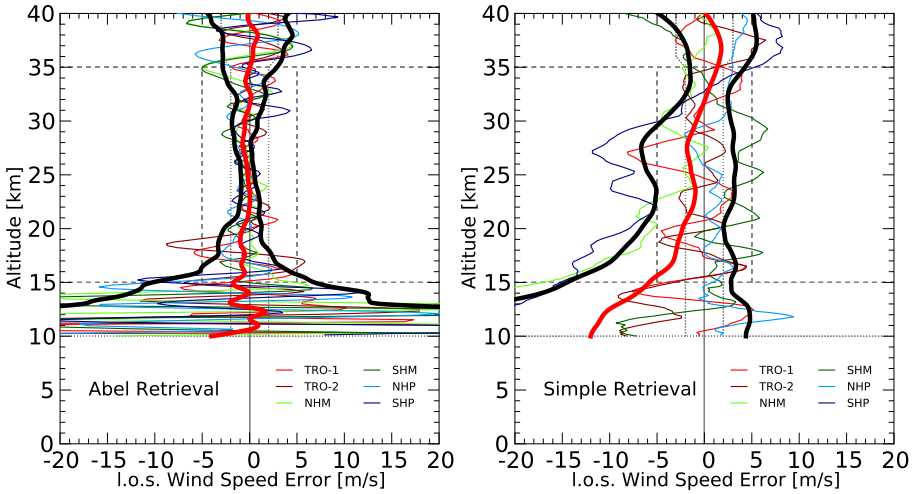

Figure 7. Statistical l.o.s wind speed errors for Abel transform retrieval (left) and simple retrieval (right) for the six example cases including TRO-1/2 (light red, red), NHM (light green), SHM (green), NHP (light blue), and SHP (blue), respectively. The heavy red lines show the estimated mean error profile, the heavy black lines the estimated SDs depicted as plus/minus envelope about the mean (both the mean and the std.dev. estimate using at each vertical level a ±2 km averaging window to smooth out individual error oscillations given the small ensemble). Target/threshold requirements for the errors are shown as dotted/dashed vertical lines, target altitude ranges analogously as horizontal lines.

AMTD
8, 405–441, 2015

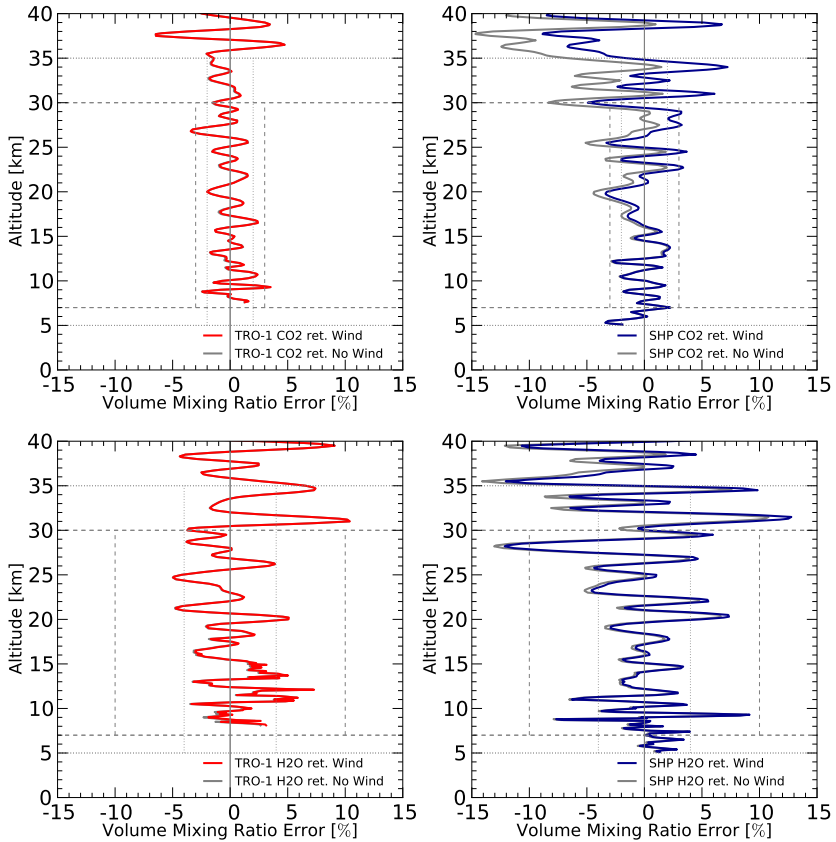

Figure 8. GHG volume mixing ratio errors with and without wind correction. The left column shows VMR results for CO_2 (top) and H_2O (bottom) for the TRO-1 case, the right column the same for the SHP case. The results without wind correction are shown as gray profiles while the results including the Doppler shift correction are shown in red (TRO-1 case) and blue (SHP case), respectively.

AMTD
8, 405–441, 2015

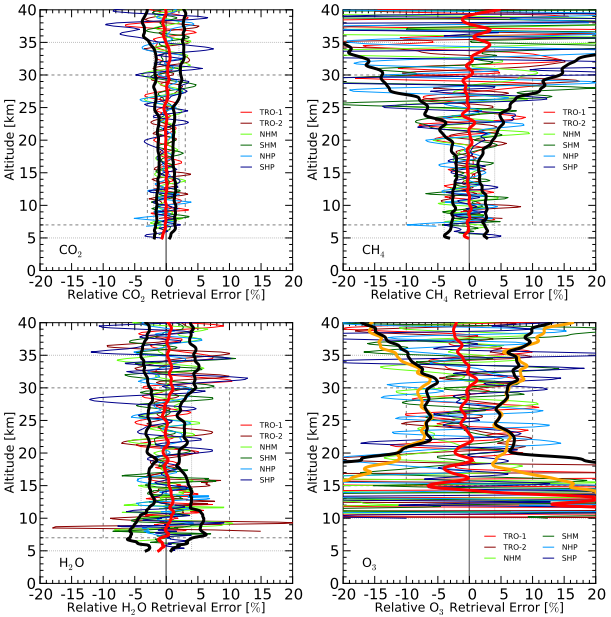

Figure 9. VMR retrieval error results for the six example cases TRO-1/2 (light red, red), NHM (light green), SHM (green), NHP (light blue) and SHP (blue), for retrievals of the GHGs CO_2 (upper left), CH_4 (upper right), H_2O (lower left), and O_3 (lower right), including the correction of wind-induced Doppler shift. The heavy red lines show the estimated mean error profile, the heavy black lines the estimated SDs depicted as plus/minus envelope about the mean (both the mean and the std.dev. estimate using at each vertical level a ±2 km averaging window to smooth out individual error oscillations given the small ensemble). For O_3 (lower right), the additional heavy orange lines mark the SD if computed from the four extratropical rather than all six cases, i.e., excluding the low-signal-to-noise-ratio cases TRO-1/2. Target/threshold requirements for the errors are shown as dotted/dashed vertical lines, target altitude ranges analogously as horizontal lines.

AMTD
8, 405–441, 2015

Wind and greenhouse gas profiling under windy air conditions

A. Plach et al.